Separation of Convective and Stratiform Precipitation Using Microwave Brightness Temperature

YE HONG

Caelum Research Corporation, Silver Spring, Maryland

CHRISTIAN D. KUMMEROW

Mesoscale Atmospheric Processes Branch, NASA/Goddard Space Flight Center, Greenbelt, Maryland

WILLIAM S. OLSON

JCET/University of Maryland Baltimore County, Baltimore, Maryland

(Manuscript received 29 September 1997, in final form 27 October 1998)

ABSTRACT

This paper presents a new scheme that classifies convective and stratiform (C/S) precipitation areas over oceans using microwave brightness temperature. In this scheme, data are first screened to eliminate nonraining pixels. For raining pixels, C/S indices are computed from brightness temperatures and their variability for emission (19 and 37 GHz) and scattering (85 GHz). Since lower-resolution satellite data generally contain mixtures of convective and stratiform precipitation, a probability matching method is employed to relate the C/S index to a convective fraction of precipitation area.

The scheme has been applied on synthetic data generated from a dynamical cloud model and radiative transfer computations to simulate the frequencies and resolutions of the Tropical Rainfall Measuring Mission (TRMM) Microwave (TMI) Imager as well as the Special Sensor Microwave/Imager (SSM/I). The results from simulated TMI data during the Tropical Ocean Global Atmosphere Coupled Ocean–Atmosphere Response Experiment agree very well with the ground-based radar classification maps. The classification accuracy degrades when SSM/I data is used, due largely to the lower spatial resolution of the SSM/I.

The successful launch of TRMM satellite in November 1997 has made it possible to test this scheme on actual TMI data. Preliminary results of TMI derived C/S classification compared with that from the first spaceborne precipitation radar has shown a very good agreement. Further verification and improvement of this scheme are under way.

1. Introduction

Precipitation is the primary exchange process within the hydrological cycle and is essential for all plant and animal life on our planet. Tropical precipitation composes more than two-thirds of the global precipitation. Through the associated latent heat release, tropical precipitation provides the major source of energy for driving the global atmospheric circulation (Simpson et al. 1988). Accurate estimates of tropical precipitation and latent heat release are thus vital for improving our understanding of the earth–atmosphere–hydrosphere system and the large-scale climate variability.

Tropical precipitation generally occurs in the form of organized mesoscale convective systems (MCSs). These systems are characterized by two distinguishable components: convective and stratiform (C/S) regions (Zipser 1977; Leary and Houze 1979; see Houze 1989 for the detailed descriptions of MCSs). Convective regions range from a few km to about 30 km in scale and have strong updrafts and downdrafts. These regions are associated with heavy precipitation and vertical air motions much larger than the typical fall velocities of ice crystals. In contrast, stratiform precipitation has relatively weak vertical air motion and greater horizontal homogeneity. It may extend for hundreds of kilometers, but it is associated with generally low rain rates that rarely exceed 10 mm h^{-1}. Besides the aforementioned differences in rainfall characteristics between convective and stratiform precipitation, the two regimes also have considerably different vertical profiles of latent heat release.

Figure 1 shows a schematic diagram of the latent heating associated with convective and stratiform pre-

Corresponding author address: Dr. Ye Hong, Code 912, NASA/GSFC, Greenbelt, MD 20771.
E-mail: yhong@agnes.gsfc.nasa.gov

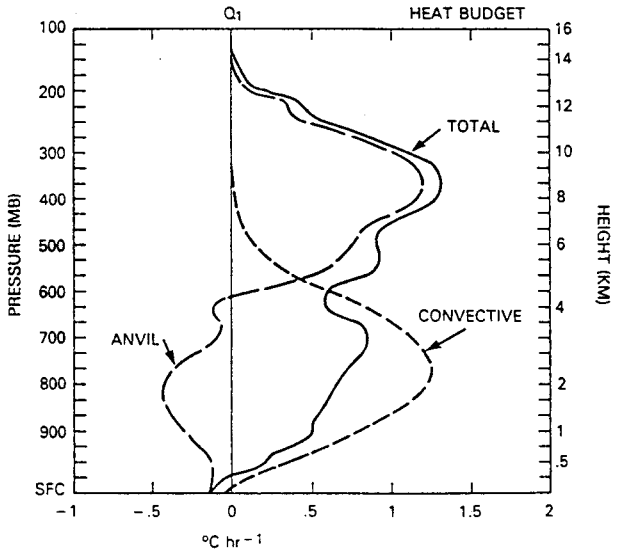

FIG. 1. Schematic diagram showing differences between latent heating profiles of convective and stratiform precipitation (from Tao and Simpson 1989).

cipitation. The convective regime can be seen to heat the entire troposphere. It is dominated by condensation/deposition processes (Tao and Simpson 1989; McCumber et al. 1991). In contrast, the stratiform region generally cools the lower troposphere as it is dominated by evaporative cooling. Tao et al. (1993) found that large-scale heating and cooling can be attributed primarily to the fraction of convective and stratiform precipitation rather than details of the cloud environment. Thus, classifying convective and stratiform regions is necessary for retrieval of latent heating release.

Although ground-based and aircraft radars have long been used to study the tropical convective systems, the need for global characterization clearly drives the problem toward satellite-based observation. Classification of cloud types using satellite data has been studied by many researchers. Shenk et al. (1976), Reynolds and Vonder Haar (1977), Adler and Negri (1988) and Rossow and Schiffer (1991) identified cloud types from visible and infrared satellite data. Alishouse et al. (1990) and Greenwald et al. (1993) used microwave satellite data to study cloud liquid water path. Since visible/infrared data give information only of cloud-top properties while microwave data has historically been limited due to poor spatial resolutions, Liu et al. (1995) developed a cloud classification scheme by combining satellite infrared and microwave data. This scheme combines information of cloud-top characteristics from the infrared data with precipitation information from the microwave data.

The aforementioned cloud classifications using microwave or combined infrared/microwave data, however, are generally rainfall retrieval schemes. As such, classifications are intended to maximize correlations in the retrieved rainfall while their validity for cloud type classification has gone untested. Anagnostou and Kummerow (1997) (AK97) developed a microwave brightness temperature-based convective/stratiform classification scheme that is independent of any rainfall retrieval scheme. They related variability of brightness temperature (T_B) from the Special Sensor Microwave/Imager (SSM/I)85 GHz to the stratiform fractional precipitation coverage over the satellite field of view (FOV) and show that the frequency of stratiform fraction of the satellite FOV rainfall coverage decreases with the increase of variability of brightness temperature.

An alternate method of determining the precipitation type from passive microwave radiation has been the use of multifrequency profiling algorithms as described by Kummerow and Giglio (1994a,b), Smith et al. (1992), and Mugnai et al. (1993). Since the vertical distributions of hydrometeors in convective precipitation regimes are different from those in stratiform precipitation regimes, these techniques should, in principle, be able to separate the two types of precipitation. While aircraft results presented in Kummerow and Giglio make it clear that this is, in fact, the case, such success is not obvious when the algorithms are applied to SSM/I data. The degradation of results is most likely due to the smaller dynamic range of the T_B signal caused by the mixing of various precipitation types in the relatively large footprints of the SSM/I. Additional information regarding the nature of the precipitation based upon textural information might thus be useful to these types of algorithms when the spatial resolution is less than adequate.

Before developing C/S separation schemes that are useful at satellite resolutions, it is useful to examine typical rainfall distributions as a function of footprint size. The data presented in Fig. 2 correspond to shipborne radar data from the Tropical Ocean Global Atmosphere Coupled Ocean–Atmosphere Response Experiment (TOGA COARE) for which surface rainfall data and convective/stratiform rainfall maps are available at 2-km resolution (see Short et al. 1995). Figure 2 shows the normalized histograms (dash lines) and rainfall volumes (solid lines) that are collected for three categories of precipitation based on the percentage of convective rain area. The three categories have fractional convective precipitation coverage of 0%–30%, 40%–70% and 70%–100%, respectively. From Fig. 2a, in which precipitation is either convective or stratiform at the processed radar resolution of 2 km, one can see that the convective precipitation volume takes about 70% of total precipitation volume while the number of stratiform precipitation pixels is about 70% of total. Relatively small convective precipitation regions contribute the most to the total rainfall volume. As expected, stratiform precipitation always occurs more frequently than convective precipitation at any resolution. As resolution degrades, mixed rainfall areas and volumes increase gradually. At 6 km, which is about the scale of the Tropical Rainfall Measuring Mission's (TRMM) highest resolution passive microwave channel (85 GHz), the contribution of rainfall volume by mixed regions is

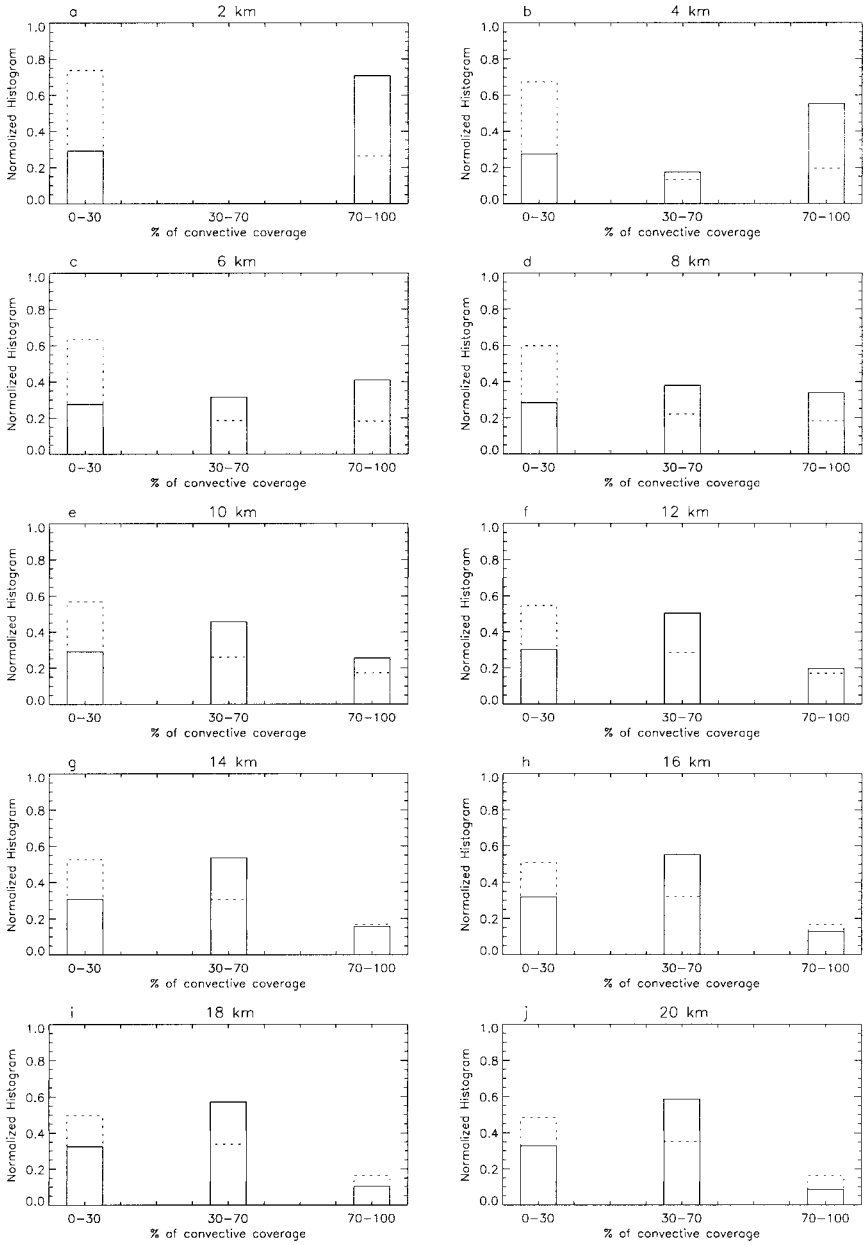

FIG. 2. Normalized frequency histograms (dash lines) and rainfall amounts (solid lines) of convective and stratiform vs percentages of convective precipitation area for different resolutions.

about 30%. The mixed precipitation increases to about 50% at 12 km, which is the scale of SSM/I's 85 GHz channel.

This study follows work of AK96 whose aim was to find the probability that a given SSM/I pixel was either convective, mixed, or stratiform based upon a variability index defined as the mean absolute 85-GHz brightness temperature difference between the pixel and the eight surrounding neighbor pixels:

$$\mathrm{VI} = \frac{1}{n}\sum_{i=1}^{n} |T_{Bc} - T_{Bi}|, \qquad (1)$$

where n is the number of surrounding pixels, T_{Bc} is brightness temperature of central pixel, and T_{Bi} is brightness temperature of surrounding pixels.

In this paper, we have developed a more sophisticated C/S separation algorithm intended primarily for TRMM Microwave Imager (TMI) data, but it is equally applicable to the Advanced Microwave Scanning Radiometer (AMSR) instrument on the Japanese Advanced Earth Observing Satellite (ADEOS) and American Earth Observing System (EOS) platforms, which have very similar resolutions to TMI. The higher spatial resolution of the TMI/AMSR data allows us to incorporate additional

texture information from lower-frequency channels although the results will be seen to be still applicable to SSM/I with the understanding that about one-half the rainfall will be classified as mixed in nature.

In this study, physical arguments are used to relate texture-based indices to the probability that pixels are either convective or stratiform. At lower spatial resolutions, the radiometric signature decreases due largely to the increased likelihood that pixels are mixtures of convective and stratiform precipitation. To overcome this problem, a probability matching scheme is employed to relate the new C/S indices developed here to the probability that various mixtures of C/S precipitation, as determined from radars, are present in a satellite FOV. Validation of this scheme has been carried out by using synthetic TMI, radar data from the TOGA COARE field experiment, and collocated TRMM precipitation radar (PR) and TMI data. The datasets are described in section 2. Section 3 provides a detailed description of the development of the new C/S partitioning method. Applications of the scheme to satellite data are presented in section 4. Section 5 presents summaries and conclusions.

2. Data

A large number of datasets have been employed in the current study. They consist of ground-based radar data, airborne radar and radiometer data, spaceborne radar and radiometer data, and dynamical cloud model data as well as synthetic satellite data generated from a combination of radar and cloud model data. Synthetic satellite data are needed because this research was conducted before TMI data are available. The successful launch of TRMM satellite in November 1997 has provided us with a good opportunity to examine and validate the technique developed here.

The TOGA COARE data, upon which the present study is based, were collected during the intensive observation period from November 1992 to February 1993. The area encompassed by the study is shown in Fig. 3. Figure 3 also shows the positions of two research ships, the *Xiangyanghong #5* and the *Vickers,* which carried the TOGA and Massachusetts Institute of Technology Doppler radars, respectively. Four vertices of the polygon indicate the locations of integrated sounding systems at the islands Kavieng and Kapingamarangi and on the two research vessels *Kexue #3* and *Shiyan #2.*

Ground-based radar data were measured from the aforementioned two shipboard Doppler radars and covered the region from the equator to 5°S and 153°E to 158°E (see the square in Fig. 3). Radar reflectivities were obtained every 10 min at the resolution of 2 km × 2 km. Rainfall rates were retrieved using the *Z–R* relationship of $Z = 120R^{1.43}$ (Short et al. 1995), which corresponds to locally measured drop size distributions. Convective/stratiform rainfall maps were produced following the separation technique of Churchill and Houze (1984). A detailed description of rain-rate retrieval and C/S classification can be found in Ferrier et al. (1995), Short et al. (1995), and Kucera et al. (1995). The subset of TOGA COARE rainfall maps corresponding to the times of the SSM/I overpasses (220 maps) were used in this study.

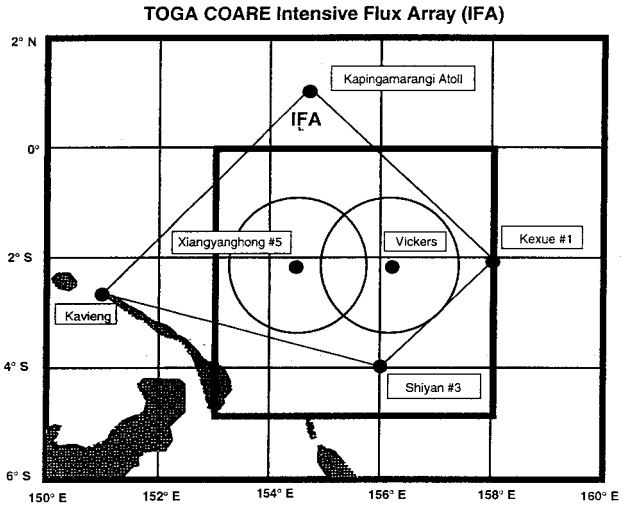

FIG. 3. TOGA COARE intensive flux array.

Coincident aircraft passive microwave data and radar data were collected from the Advanced Microwave Precipitation Radiometer (AMPR) on board the NASA ER-2 aircraft and the Airborne Rain Mapping Radar (ARMAR) on board the NASA DC-8 aircraft during TOGA COARE. AMPR and ARMAR were developed to match TRMM instruments TMI and PR, respectively. AMPR measures linearly polarized radiation at 10.7, 19.35, 37.1, and 85.5 GHz. It samples data by scanning over a ±45° in the cross-track direction. At a typical flight altitude of about 20 km, surface footprints of the AMPR are 2.8 km for 10.7 and 19.35 GHz, 1.5 km for 37.1 GHz, and 0.6 m for 85.5 at nadir view. ARMAR operates at 13.8 GHz and measures reflectivity in a cross-track scan ±20° from nadir. Its vertical resolution is 80 m with a horizontal resolution of 0.8 km at a flight altitude of 12 km. Full descriptions of those instruments and data can be found in Spencer et al. (1994) and Durden et al. (1994).

Spaceborne microwave radiometer data was obtained from the SSM/I and TMI. The SSM/I is a seven-channel four-frequency (19.35, 22.235, 37.0, and 85.5 GHz) passive microwave radiometer on board on the Defense Meteorological Satellite Program (DMSP) polar orbiting satellite. It measures radiance from the atmosphere and surface and has horizontal scales from 49 km × 60 km (19.35 GHz) to 13 km × 15 km (85.5 GHz). SSM/I data utilized in this study are from passes over the TOGA COARE region. It includes *F10* and *F11* satellites that have viewing times of about 1100 UTC and

2300 UTC (*F10*), and 0700 UTC and 1900 UTC (*F11*), respectively.

The TMI is a nine-channel passive microwave radiometer with dual polarization channels at 10.7, 19.35, 37, and 85.5 GHz and a vertical-polarization channel at 21.3 GHz. It is essentially a copy of the SSM/I with a dual-polarized pair of 10.7-GHz channels added to increase the dynamic range of rainfall estimates. In addition, the 21.3-GHz water vapor absorption channel is designed in the TMI instead of 22.235 GHz in the SSM/I to avoid saturation in the Tropics. With the TRMM satellite orbit at an altitude of 355 km, spatial resolutions of the TMI have been improved. TMI footprint dimensions range from about 40 km for 10 GHz channels to 5 km for 85.5 GHz.

The first spaceborne PR is a cross-scanning 13.8 GHz radar that has a swath width of about 220 km, about one-third of TMI's swath width. The PR provides invaluable information on three-dimensional (3D) distribution of rainfall intensity, rain type, and storm depth at a horizontal resolution of about 4.4 km and vertical resolution of about 250 m. In the present study, rainfall types (convective or stratiform) derived from 3D PR reflectivities are used as the validation for TMI derived rainfall types.

Cloud models play an important role in this study because they offer complete hydrometeor profiles along with surface rainfall rates and C/S classification based upon the vertical motions of the air columns. Classifications based upon the instantaneous 3D structure of hydrometeors can thus be compared directly to the more fundamental definition of convection. Cloud resolving models such as the Goddard Cumulus Ensemble model (GCE), which is a cloud microphysical model developed mainly by Tao and Simpson (1993), are used to supply the required atmosphere and cloud structures. The shapes of liquid and ice are assumed to be spherical. The distributions of rain, snow, and graupel (or hail) are taken to be inverse exponential with respect to the diameter (D) such that

$$N(D) = N_0 \exp(-\lambda D), \tag{2}$$

where $N(D)$ is the number of drops of diameter between D and $D + dD$ per unit volume, N_0 is the intercept parameter, and λ is the slope of the distribution given by

$$\lambda = \left(\frac{\pi \rho_x N_0}{\rho q_x}\right)^{0.25}. \tag{3}$$

The typical intercept parameters used in the GCE model for rain, snow, and graupel are 0.08 cm^{-4}, 0.04 cm^{-4}, and 0.04 cm^{-4}, respectively. The density of rain, snow, and graupel are 1 g cm^{-3}, 0.1 g cm^{-3}, and 0.4 g cm^{-3}, respectively. The cloud ice is monodisperse with a diameter of 2×10^{-3} cm and a density of 0.917 g cm^{-3}.

In order to study the expected performance of the algorithm developed in this study, synthetic data corresponding to the TMI as well as SSM/I instruments are also created. This is accomplished by combining a cloud model with observed rainfall patterns from the TOGA COARE shipborne radars (see Kummerow 1997). To begin with, mean vertical hydrometeor profiles are derived by averaging profiles from the cloud model within specified surface rainfall ranges for clear, stratiform, and convective profiles, respectively. Thirty-two convective rainfall intervals ranging from 0.5 to 120 mm h^{-1} were used for convective precipitation while 21 intervals from 0.2 to 25 mm h^{-1} were used for stratiform precipitation. These profiles are then used, in conjunction with surface rainfall and C/S classification determined by the radar, to construct probable hydrometeor fields within the radar FOV. Radiative transfer computations are then performed through the hydrometeor field created above, and the upwelling radiance are averaged to either TMI or SSM/I resolutions. While observed vertical profiles may not correspond to the average hydrometeor profiles employed in this study, such a scheme ensures at a minimum that the horizontal variability of rainfall rates is accurately captured by this dataset.

3. Convective/stratiform separation techniques

a. Radar C/S partitioning schemes

Since radar partitioning of C/S precipitation is used throughout this study, a brief review of those separation techniques is presented first. Houze (1993) defined convective and stratiform precipitation in terms of their vertical velocity scales. Namely, the vertical velocity of air (~1–3 m s^{-1}), is smaller than the fall velocity of ice in stratiform precipitation while vertical air speed (~1–10 m s^{-1}) in convective precipitation is larger than the fall velocity of ice. Using mass continuity arguments, a change in vertical velocity must be associated with change in the horizontal mass field. Without conventional data of vertical velocity, therefore, the horizontal structure of radar reflectivities has been widely used for separating C/S precipitation.

The most popular radar C/S separation approach is classifying precipitation as stratiform if the radar reflectivity bright band exists (Collier et al. 1980; Rosenfeld et al. 1995). However, this method has its limitations because the bright band is not clearly exhibited in early or late stages of development of stratiform precipitation (Yuter and Houze 1995). Even though the bright band exists in stratiform precipitation, it may not be detected by ground-based radar due to the scan geometry. Therefore, Churchill and Houze (1984) (CH84), Steiner and Houze (1993), and Steiner et al. (1995) have developed an algorithm that uses the horizontal structure of the precipitation field to distinguish between convective and stratiform precipitation. Using radar data with 4-km horizontal resolution, CH84 first identify any grid point of which reflectivity is greater than 40 dBZ as a convective center. Next a grid point with reflectivity of less than 40 dBZ is also considered as a convective

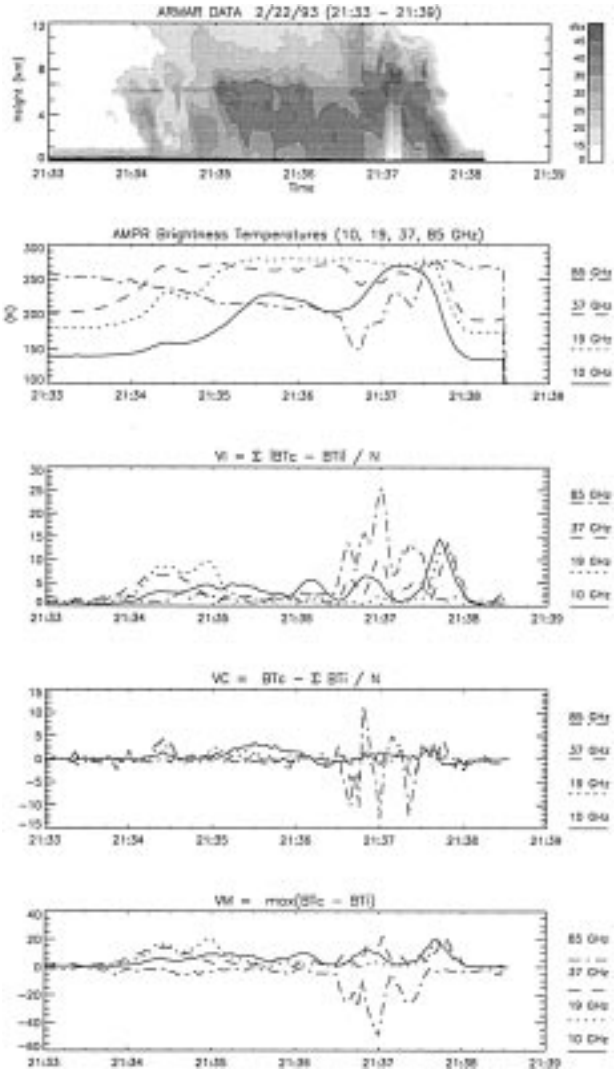

FIG. 4. A squall line on 22 Feb 1993 at the original data resolution (a) radar reflectivities from ARMAR; (b) brightness temperatures from AMPR for 10 GHz, 19 GHz, 37 GHz, and 85 GHz; (c) VI for four channels; (d) VC for four channels; (e) VM for four channels.

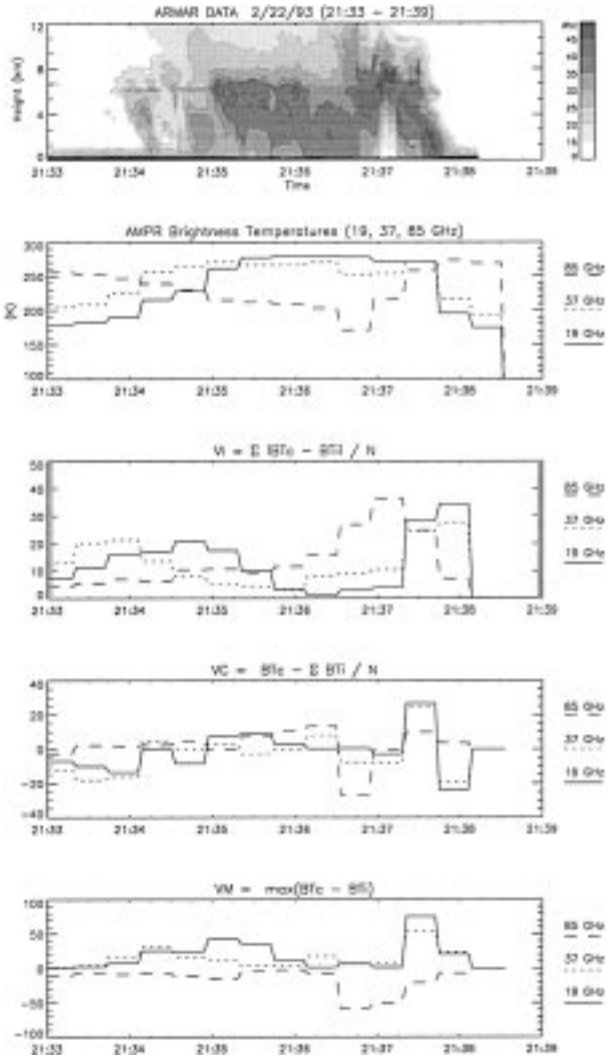

FIG. 5. Same as in Fig. 4 except at the TMI's resolution; 10-GHz data are not shown.

center if the difference between its reflectivity and the average reflectivity of surrounding background (400 km^2) exceeds a peakness threshold of 4.0 dBZ. Finally, all surrounding grid points of a convective center are considered as convective regions.

Following CH84's algorithm, Short et al. (1995) have generated convective/stratiform rainfall maps from shipborne radar data during TOGA COARE. The rain rates at each grid are first derived using the Z–R relationship of $Z = 120R^{1.43}$. If the rain rate of the central grid is more than twice the average rain rate of the surrounding 24 pixels, the central point and its nearest eight neighbors are classified as convective. All grids with values greater than 20 mm h^{-1} (about 40 dBZ) are further identified as convective centers. The C/S maps generated in this method correspond to the official TOGA COARE products and are used in current study.

The classification of convective/stratiform precipitation using spaceborne PR data are based on both vertical profile method and horizontal pattern technique. Dr. J. Awaka (1998, personal communication) at Hokkaido Tokai University, Japan, checked if the radar reflectivity bright band exists to determine the first set of rain type data. Then he applied the aforementioned horizontal structure method to obtain the second set of convective/stratiform precipitation data. The unified rain types are obtained by combining both results.

b. Development of satellite microwave C/S index (CSI)

Like radar reflectivities, passive microwave T_Bs respond directly to the hydrometeors in clouds. How-

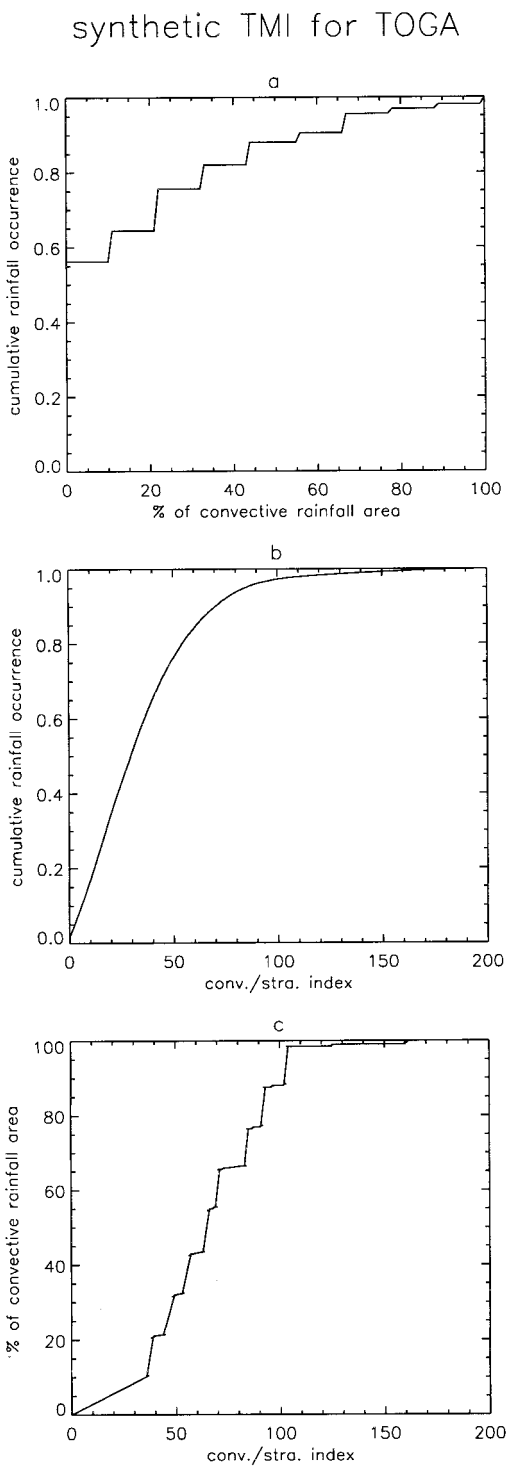

FIG. 6. (a) Cumulative distribution functions of fractional convective precipitation from radar data, (b) C/S index from simulated TMI data, and (c) fractional convective precipitation vs C/S index.

ever, diffraction has limited the resolution of a spaceborne radiometer. Compared to ground-based radar data that have typically utilized 2-km data, the 19-GHz data from the SSM/I have a resolution of 43 km $\times$ 60 km. Thus, radar C/S separation techniques cannot be simply applied to microwave T_Bs. Nonetheless, microwave brightness temperature separation of C/S precipitation must be based upon some physically meaningful quantities. We begin by investigating the behavior of some indices designed to capture the textural information in the microwave T_B signal at high spatial resolutions.

At 85 GHz, passive microwave T_Bs are sensitive primarily to the precipitation ice content in clouds. The variability of 85 GHz is thus a good indicator of convection. McGaughey et al. (1996), however, found that in tilted convective systems, there is often ice aloft in stratiform regions with only light rain below and shallow heavily raining clouds with little ice above. Thus, information from only the 85-GHz channel may not correctly separate convective from stratiform precipitation in tilted convective system or other convective systems, such as warm convection where there is little ice aloft. In contrast, microwave brightness temperatures at 10 and 19 GHz are physically related to liquid hydrometeors in clouds and surface rainfall. If not for their poor spatial resolution, these channels in fact would contain far more information regarding the actual variability of the rainfall. Since each frequency appears to have its own set of limitations, a combination of both emission and scattering channels is investigated.

To examine the brightness temperature features of a convective region, simulated TMI data are investigated. As mentioned earlier, GCE cloud model provides complete hydrometeor profiles along with surface rainfall rates and C/S classifications. Synthetic TMI brightness temperatures can be generated by utilizing radiative transfer computations through the cloud model atmosphere at the TMI frequencies. The other simulated TMI data were from aircraft-borne AMPR data that have the same channels as TMI.

Three variability indices of brightness temperatures have been examined. The first one, VI, is the same as used by AK96 and given in Eq. (1). The second one, VC, is defined as the brightness temperature difference between the center pixel and the averaged value of the surrounding pixels,

$$\mathrm{VC} = T_{Bc} - \frac{1}{n}\sum_{i=1}^{n} T_{Bi}, \tag{4}$$

where n, T_{Bc}, and T_{Bi} are the same as those in Eq. (1).

The third one, VM, is the maximum temperature enhancement due to emission for the 19- and 37-GHz channels or the maximum depression due to scattering at 85 GHz. VM is given by

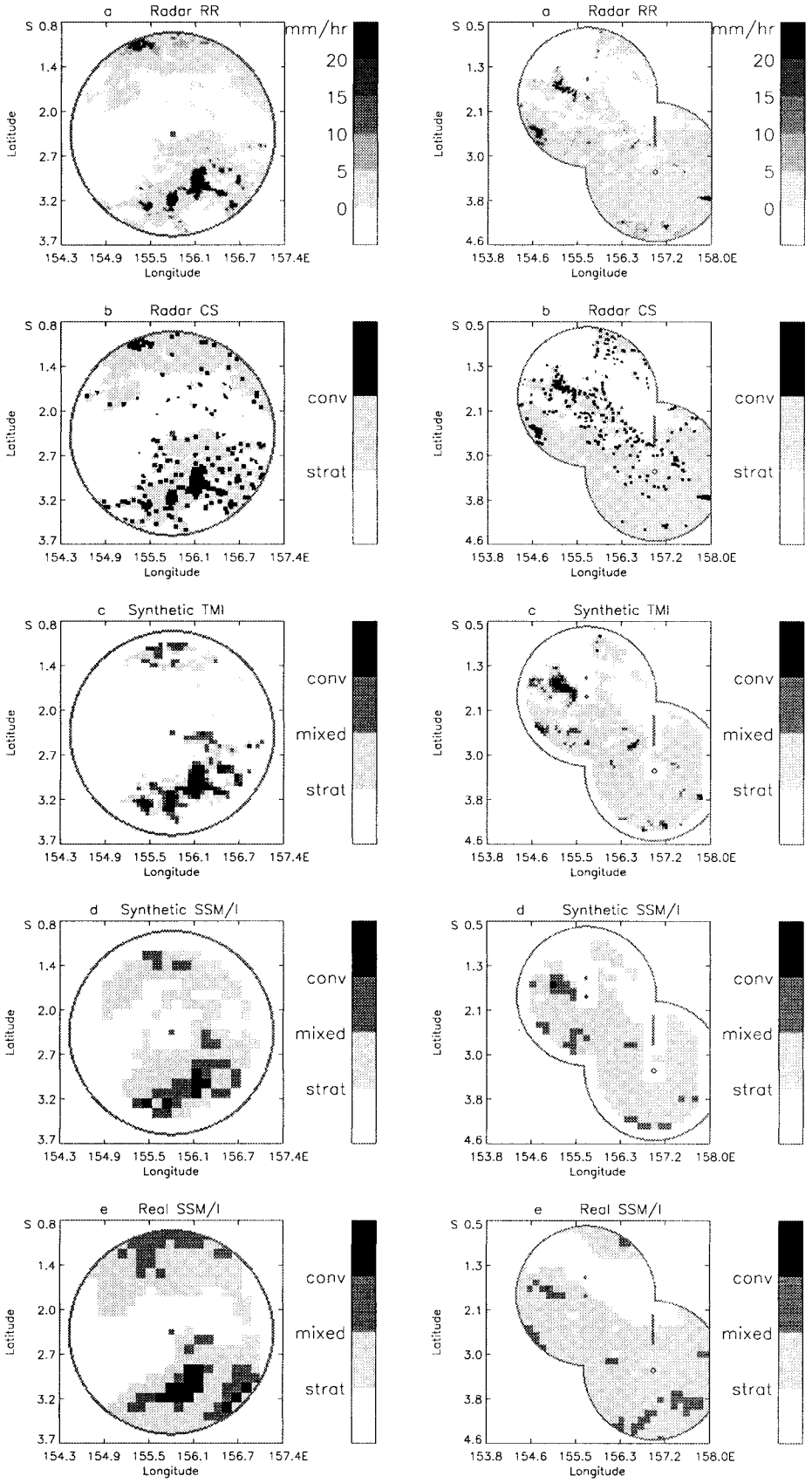
a Radar RR
mm/hr
20
15
10
5
0
b Radar CS
conv
strat
c Synthetic TMI
conv
mixed
strat
d Synthetic SSM/I
conv
mixed
strat
e Real SSM/I
conv
mixed
strat
Latitude
Longitude
S 0.8
1.4
2.0
2.7
3.2
3.7
154.3 154.9 155.5 156.1 156.7 157.4E
S 0.5
1.3
2.1
3.0
3.8
4.6
153.8 154.6 155.5 156.3 157.2 158.0E

$$\mathrm{VM} = \mathrm{Max}(T_{Bc} - T_{Bi}) \geq 0 \quad \text{for 19 or 37 GHz}$$

or

$$\mathrm{VM} = \mathrm{Min}(T_{Bc} - T_{Bi}) \leq 0 \quad \text{for 85 GHz.} \tag{5}$$

Figure 4 displays a squall line observed in the TOGA COARE IFA on 22 February 1993. In Figs. 4a and 4b, the radar reflectivities from ARMAR and coincident brightness temperatures at nadir from AMPR are shown, respectively. As can be seen, a convective region appears between time at about 2137:50 and 2138 UTC. The value T_{B10} gives the best indication of a convective region while T_{B19} is saturated and shows little difference between stratiform and convective regions. In addition, the lowest T_{B85} is shifted from the highest T_{B10}, which suggests that convection is tilted. Figure 4c–e show the three computed variability indices. While signals are somewhat noisy, large variability indices can be seen to correlate very well with the convective areas identified by the radar.

To simulate TMI resolution, the data are averaged to 4.8 km, 12 km, and 22.4 km for 85 GHz, 37 GHz, and 19 GHz, respectively. Although the 10-GHz data have a larger dynamic range than other emission channels, they are not considered in the current study due to their low spatial resolution from the spaceborne TMI. Figure 5a–e are the same as in Fig. 4a–e except that brightness temperatures are at TMI's resolutions. Clearly, variability indices at the lower resolution exhibit clearer features in the convective region than do the brightness temperatures. This occurs because the scale of the convective core is closer to the scale of the TMI observations than that of the original data resolution. But peaks of VI are shifted from those of brightness temperature since VI gives the gradient of brightness temperature. In this study, variability of VM is used instead of VI in the C/S separation index. There are several advantages to this change. First, VM can amplify the signal when the center pixel covers a convective region. This is important for low resolution channels of 19 GHz and 37 GHz because their FOVs for the TMI are equivalent to or larger than the scale of convective regions. Features in one FOV may have been smoothed while VI gives only average information. Second, the peak of VM corresponds the peak of brightness temperature so that the implied convective regions will not be shifted. Third, VM ensures that high variability results only from high brightness temperatures due to emission or low brightness temperatures due to scattering.

The VM, however, is sensitive to the quality of the data. Any bad data point in the surrounding pixels (for example, one single high or low brightness temperature) will cause a false convective signal. To reduce such errors, screening data (quality check, raining pixels check) is necessary before separating C/S regions. The intensity of a signal may also be added to the CSI to minimize its sensitivity to data quality. The CSI is defined separately for emission and scattering as follows: for emission,

$$\mathrm{CSI}_e = 0.5 \times \mathrm{VM}_{19} + \mathrm{VM}_{37} + 0.25(T_{B19} - T_{B19\mathrm{bg}}) \tag{6}$$

and for scattering,

$$\mathrm{CSI}_s = \mathrm{abs}(\mathrm{VM}_{85}) + (T_{B85\mathrm{bg}} - T_{B85}), \tag{7}$$

where $T_{B19\mathrm{bg}}$ and $T_{B85\mathrm{bg}}$ are background brightness temperatures for 19 GHz and 85 GHz, respectively. The reduced weight given to VM19 relative to VM37 is due to its lower resolution. Both emission and scattering information are supplied by 37-GHz data. Since 85-GHz data provide better scattering information than the 37-GHz channel, only emission information from 37-GHz data is utilized for current study. The $0.25(T_{B19} - T_{B19\mathrm{bg}})$ term in Eq. (6) not only amplifies the convective characteristic but also compresses the possible false signals resulting from any bad surrounding pixels' data. To remove the effect of the background, the background brightness temperature is subtracted from the brightness temperature of the pixel for the 19-GHz channel in Eq. (6) and the 85-GHz channel in Eq. (7).

By combining CSI_e and CSI_s, the CSI becomes

$$\mathrm{CSI} = (1 - w)\mathrm{CSI}_e + w\,\mathrm{CSI}_s, \tag{8}$$

where w is the weight based on scattering information and is defined by

$$w = \begin{cases} 0 & \text{if } T_{B85} > T_{B85\mathrm{bg}} \\ (T_{B85\mathrm{bg}} - T_{B85})/80 & \text{if } T_{B85\mathrm{bg}} - 80 < T_{B85} < T_{B85\mathrm{bg}} \\ 1.0 & \text{if } T_{B85} < T_{B85\mathrm{bg}} - 80. \end{cases} \tag{9}$$

In other words, the variability of 85-GHz ice scattering determines CSI when significant ice is present while the variability of both the 19- and 37-GHz emission channels determines CSI when no ice is present. The CSI reflects the variability and intensity of brightness temperature. Two indices each for emission and scattering can compensate for each other's disadvantages. The scattering index alone has indirect relation to the surface rainfall. More ice (low T_{B85}) suggests high surface rainfall, but less ice does not imply low surface rainfall if it is a warm or tilted convection. Emission index has the direct response to surface rainfall, but the

←

FIG. 7. Case 1: the MCS during TOGA COARE at 1101 UTC on 20 Dec 1992. (a) The radar rainfall map; (b) the radar C/S map; (c) the C/S map from synthetic TMI data; (d) the C/S map from synthetic SSM/I data; and (e) the C/S map from actual SSM/I data.

FIG. 8. Same as in Fig. 7 except for the case of the MCS at 1841 UTC on 20 Dec 1992.

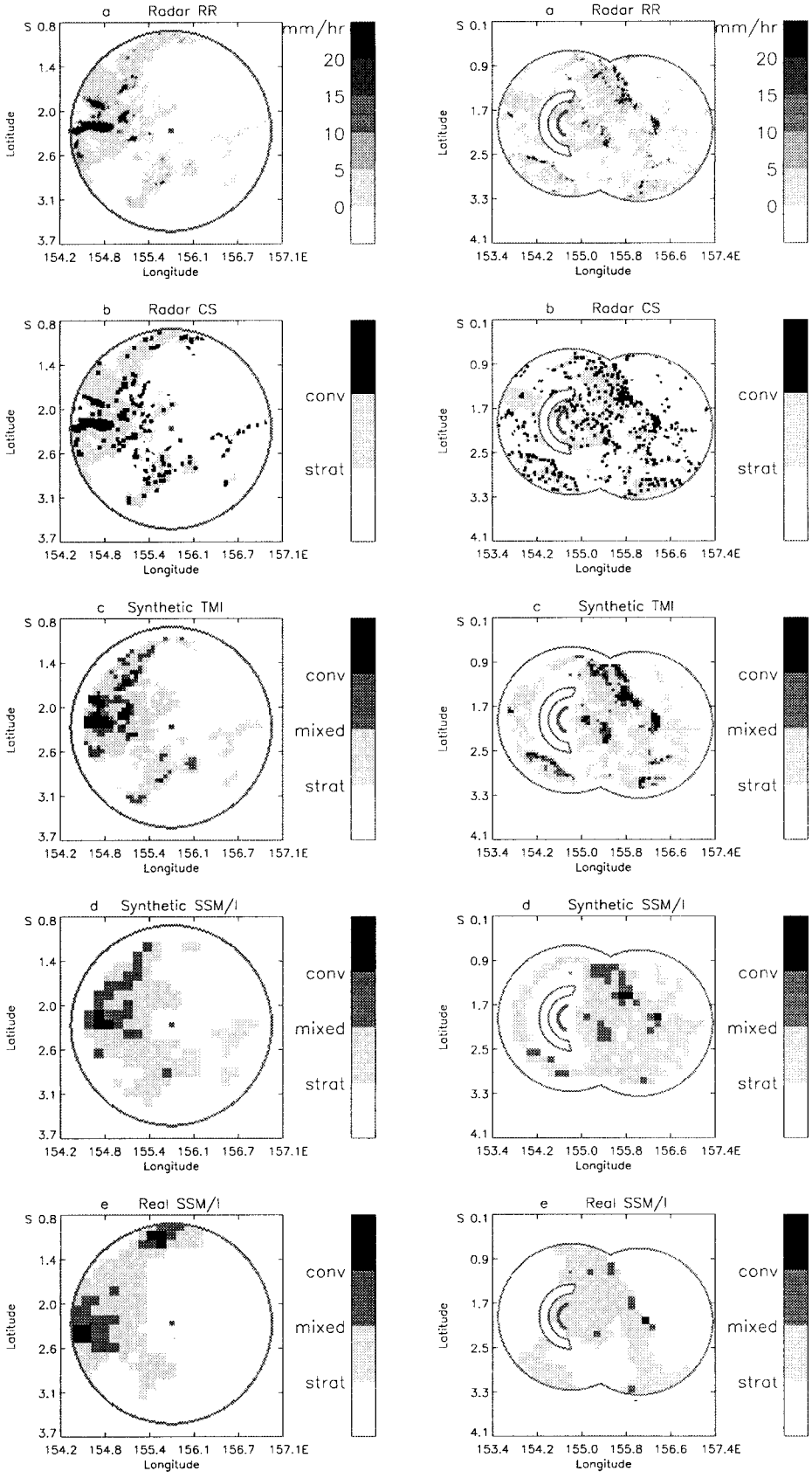
a Radar RR
mm/hr
20
15
10
5
0
b Radar CS
conv
strat
c Synthetic TMI
conv
mixed
strat
d Synthetic SSM/I
conv
mixed
strat
e Real SSM/I
conv
mixed
strat
Latitude
Longitude
S 0.8
1.4
2.0
2.6
3.1
3.7
154.2 154.8 155.4 156.1 156.7 157.1E
S 0.1
0.9
1.7
2.5
3.3
4.1
153.4 154.2 155.0 155.8 156.6 157.4E

data have lower resolutions and will saturate at high rain rate.

c. Classification scheme

The previous section discusses the physical connection between CSI and the probability that a given pixel is convective. It does not, however, assign quantitative values to CSI depending upon the nature of the precipitation. A probability matching scheme (see Calheiros and Zawadzki 1987; Rosenfeld et al. 1993) is used instead to solve this problem. This scheme matches probability distribution functions of the convective fraction of precipitation area derived from ground radar reflectivity and the convective/stratiform index derived from satellite microwave brightness temperature. The fraction of convective precipitation area is the ratio of convective rainfall pixels to total pixels in a satellite 85-GHz footprint. The C/S index is computed using Eq. (8).

The high-resolution ground-based radar data are averaged to the spatial resolution of the satellite data under investigation, and a cumulative distribution function (CDF) of precipitation is created as a function of the fraction of convective rainfall area. Cumulative distribution function of precipitation is then computed as a function of CSI, which is calculated from the collocated satellite data. The two CDFs are matched in order to derive the fraction of convective rainfall area as a function of CSI. Figures 6a and 6b show such a pair of CDFs derived from synthetic TMI data during TOGA. The discontinuity in Fig. 6a is a consequence of the fact that only nine radar pixels are contained in a TMI 85 GHz's footprint. Thus the fraction of convective precipitation is multiples of one-ninth. Figure 6c displays the curve relating the CSI to the fraction of convective precipitation. As can be seen, a CSI of 80 corresponds the fraction of convective rainfall area about 70%. Each CSI corresponds a certain fraction of convective precipitation. C/S indices less than 40 and greater than 100 correspond to 90% stratiform and 90% convective, respectively.

Once the match between the fractional convective precipitation and the CSI is established, application of the procedure to satellite data can be summarized as follows.

Step 1. Determine the background brightness temperature for each channel.
Step 2. Find possible raining pixels.
Step 3. Compute C/S indices [see Eqs. (5)–(19)], and assign convective precipitation fraction based upon probability matching scheme for each raining pixel.

It is important to mention that this separation technique is partially based on the horizontal structure of precipitation and thereby is sensitive to the horizontal scale. As Steiner et al. (1995) described in their paper, ''when the algorithm is designed for a lower-resolution grid, it identifies too much area as convective if run on a higher grid resolution, since the higher-resolution data reveal more details in the reflectivity pattern—and vice versa.'' The probability matching curves, therefore, need to be generated for each particular resolution.

4. Application

The described C/S separation scheme is first applied to convective cases during TOGA COARE using synthetic TMI data. The successful launch of the TRMM satellite in November 1997 has allowed us to test the scheme on preliminary TMI data. The classification results from synthetic TMI data and real TMI data are validated against ground-based radar data and PR data, respectively.

Although this scheme is developed for TMI data that have a better resolution than SSM/I data, the availability of well-calibrated SSM/I data with long period prompts us to test this scheme. As discussed earlier, current convective/stratiform scheme is sensitive to resolution. To overcome this problem and apply the scheme to SSM/I data, two modifications of the scheme have been made: 1) the CSI consists of CSI_s only because of lower resolutions of SSM/I's 19-GHz and 37-GHz channels; 2) CDF curves are reconstructed based on the SSM/I's resolution. The applications of the C/S separation scheme to SSM/I data, as well as its validation, are based on TOGA COARE data only.

a. Synthetic TMI data

Synthetic satellite brightness temperature data were generated for TOGA radar data at the resolution of 2 km $\times$ 2 km using the procedure described previously. To simulate TMI data, brightness temperatures are averaged over 6 km $\times$ 6 km (3 $\times$ 3 radar pixels) for 85 GHz, 12 km $\times$ 12 km for 37 GHz, and 20 km $\times$ 20 km for 19 GHz, respectively. For simplicity, a TMI FOV is assumed to have rain if there is at least one raining radar pixel in the FOV of 6 km $\times$ 6 km.

In order to verify the scheme, synthetic TMI data are divided into two parts: one for creating cumulative distribution function and the other for testing. There were about 220 overpasses of F10 and F11 SSM/I data over TOGA COARE radar sites. Synthetic TMI data from the time periods corresponding to every other SSM/I overpass were used to construct CDF curves. Since con-

←

FIG. 9. Same as in Fig. 7 except for the case of convection at 2221 UTC on 16 Dec 1992.

FIG. 10. Same as in Fig. 7 except for the case of convection at 0711 UTC on 15 Feb 1993.

TABLE 1. Matched percentages of total rainfall areas and volumes for synthetic TMI data (case 1).

Radar reflectivity scheme	Brightness temperature scheme					
	Percent of rainfall areas			Percent of rainfall volumes		
	Convective	Mixed	Stratiform	Convective	Mixed	Stratiform
Convective	5.63	0.00	1.24	65.33	0.00	0.27
Mixed	3.44	4.81	11.26	10.73	5.85	2.45
Stratiform	0.41	8.10	65.11	0.57	5.40	9.40

secutive overpasses are at least 4 h apart, the datasets used for constructing the CDF curves and testing them are considered to be independent. Cumulative rainfall occurrence histograms are collected from TOGA COARE radar data as a function of convective precipitation fraction at the resolution of 6 km × 6 km. Cumulative rainfall occurrence histogram as a function of CSI is computed from synthetic TMI data. These two histograms are shown in Fig. 6a and 6b.

As discussed previously, a given CSI corresponds to a fraction of convective precipitation (see Fig. 6c). In order to compare the classificaton results qualitatively and quantitatively with those derived from radar, a satellite FOV is considered to be ''convective'' if more than 70% of the area is covered by convective precipitation while an FOV in which less than 30% of the area is convective will be classified as a ''stratiform.'' Intermediate percentages are classified as ''mixed.'' Therefore, satellite pixels with CSI values larger than about 80 would be considered as convective, while stratiform would be assigned to satellite pixels that have CSI values less than about 50. Other raining pixels are categorized as mixed.

Figures 7–10 display C/S classification maps for four TOGA cases. Rain rates and C/S maps produced from radar reflectivities are also displayed. A short vertical line in Figs. 8a–e and two C-shaped regions in Fig. 10a–e are caused by missing radar data. For comparison, C/S maps derived from SSM/I data are shown on each figure, but will be discussed later. Detailed quantitative comparison results are listed in Tables 1–4, which give percentages of matched classification areas and rainfall amounts at the resolution of 6 km × 6 km.

Case 1 (Fig. 7) and case 2 (Fig. 8) are both MCS on 20 December 1992. Case 1 is in the early development stage of the MCS in which large convective precipitation is present, while case 2 is in the late development stage that stratiform precipitation dominates. In case 1, about 5.63% of the raining areas, which correspond to 65.33% of the total rainfall amount, are classified as convective by both schemes. The areas classified as stratiform by both schemes make up about 65.11% of the total raining area corresponding to about 9.40% total rainfall volume. Some of the radar-claimed mixed areas have been considered as convective or stratiform by satellite brightness temperature scheme. These misclassified areas make up about 3.44% and 11.26% of total rain area, respectively, for convective and stratiform, while their corresponding rainfall volumes are about 10.73% and 2.45% of the totals, respectively. The overestimation and underestimation of convective areas by satellite schemes may be explained by the low-resolution brightness temperature data available. In edges of organized convective systems, satellite FOVs cover both heavy rainfall areas and nonrain areas. Thus, the convective rainfall fraction in a satellite FOV may be less than 70% but the C/S index derived from the FOV-averaged T_B is large enough to indicate that convection is possible. On the contrary, underestimated convective areas are generally those scattered convective areas that have small horizontal scales (see Figs. 7b and 7c) or light rainfall (see Figs. 7a and 7c). In case 2, about 81.25% of the raining areas, which correspond to about 48.55% of the total rainfall volume, are classified as stratiform by both schemes. Once again, brightness temperature scheme underestimates small and scattered convective regions.

Case 3 (Fig. 9) is a convective case on 16 December 1992. In this case, about 68% of the total rainfall area (~77% of the rainfall volume) were separated correctly in terms of the radar's classification. Case 4 (Fig. 10) presented another MCS on 15 February 1993, in which percentages of correct separation were about 68% for rainfall area and 64% for rainfall volume. In both cases, there were more than 2.5% of the rain areas that were classified as convective by radar scheme but stratiform

TABLE 2. Matched percentages of total rainfall areas and volumes for synthetic TMI data (case 2).

Radar reflectivity scheme	Brightness temperature scheme					
	Percent of rainfall areas			Percent of rainfall volumes		
	Convective	Mixed	Stratiform	Convective	Mixed	Stratiform
Convective	1.39	0.29	1.27	21.05	1.00	0.96
Mixed	1.33	1.16	9.32	10.87	3.28	4.68
Stratiform	0.12	3.88	81.25	0.39	9.22	48.55

TABLE 3. Matched percentages of total rainfall areas and volumes for synthetic TMI data (case 3).

Radar reflectivity scheme	Brightness temperature scheme					
	Percent of rainfall areas			Percent of rainfall volumes		
	Convective	Mixed	Stratiform	Convective	Mixed	Stratiform
Convective	5.81	0.00	2.72	61.75	0.00	1.01
Mixed	3.63	5.27	13.97	11.01	5.50	3.22
Stratiform	0.18	11.43	56.99	0.26	7.80	9.45

by the brightness temperature schemes. It indicates that the low-resolution satellite brightness temperature data do not capture the small-scale convection seen in the radar figures.

The scheme has been applied to those synthetic TMI data that are not used for constructing probability matching curves. Comparison with ground-based radar data shows those percentages of total misclassification range from 1% to 10%. The total misclassification areas are those that are classified as convective (or stratiform) by the radar scheme but as stratiform (or convective) by the brightness temperature scheme. As displayed in the above four cases, the new scheme successfully classifies organized convective systems. The percentages of total misclassification in those cases are less than 3%. However, results also show that the percentages of semimisclassification range from 10% to 30%. The semimisclassification areas are defined as those that are classified as mixed (convective or stratiform) by the radar scheme but as stratiform or convective (mixed) by the brightness temperature scheme. As discussed earlier, the low resolution may be the major factor that causes the scheme to underestimate scattered convective areas and overestimate edges of organized convective systems. In addition, the synthetic TMI data are computed from averaged profiles in which features may have been smoothed by averaging so that the underestimation occurs. Moreover, the variability index tends to be exaggerated at the edge of a rain area that may lead to the overestimation of convective areas.

b. Actual TMI data

The scan geometry of TMI and PR needs to be described before actual TRMM data are applied to the scheme. The TMI samples every 9 km alongscan for channels 10.7, 19.35, 21.35, and 37 GHz and every 4.5 km alongscan for channels 85.5 GHz, while along track it samples every 14 km for all channels. The footprint size of 85-GHz channels is about 5 km $\times$ 7 km. The PR has a horizontal footprint dimension of 4.3 km, and it samples every 4.4 km both alongscan and along track. Figure 11 shows the scan geometry of both instruments. For each TMI pixel, the fraction of convective area is derived as follows:

$$\text{convFrac} = \sum (\text{wgt}_i \times \text{prCSI}_i) \Big/ \sum \text{wgt}_i, \quad (10)$$

where the prCSI_i is C/S index for a PR pixel that is located fully or partially in a TMI footprint. The index is assigned 0 for stratiform and 1 for convection as provided by the TRMM standard products. The wgt_i is the Gaussian function based on the distance between centers of a PR pixel and the TMI footprint.

The TMI data are first screened to eliminate nonraining pixels by applying rainfall screening routines available from most rainfall retrieval schemes. This study used the screening method described by Kummerow and Giglio (1994a). The C/S index of each raining pixel is computed using Eqs. (6)–(9). To examine and compare the CDF curves with those from synthetic data, a cumulative oceanic rainfall occurrence histogram as a function of CSI is computed from TMI data for March 1998 (Fig. 12a). Cumulative oceanic rainfall occurrence histograms are also collected from PR data as a function of convective precipitation fraction derived from Eq. (10) (Fig. 12b). Figure 12c is for convective fraction versus CSI obtained from matching two cumulative rainfall occurrence histograms (Fig. 12a and 12b). Very similar curves can be seen in Fig. 12c from the real TMI data and in Fig. 6c from the simulated TMI data.

As in the previous section, a TMI pixel is considered as convective/mixed/stratiform according to the fraction of convective precipitation in its footprint. The con-

TABLE 4. Matched percentages of total rainfall areas and volumes for synthetic TMI data (case 4).

Radar reflectivity scheme	Brightness temperature scheme					
	Percent of rainfall areas			Percent of rainfall volumes		
	Convective	Mixed	Stratiform	Convective	Mixed	Stratiform
Convective	4.41	1.88	2.62	44.22	3.69	1.64
Mixed	3.66	5.82	20.16	16.99	12.51	8.31
Stratiform	0.19	3.19	58.07	0.59	4.61	7.45

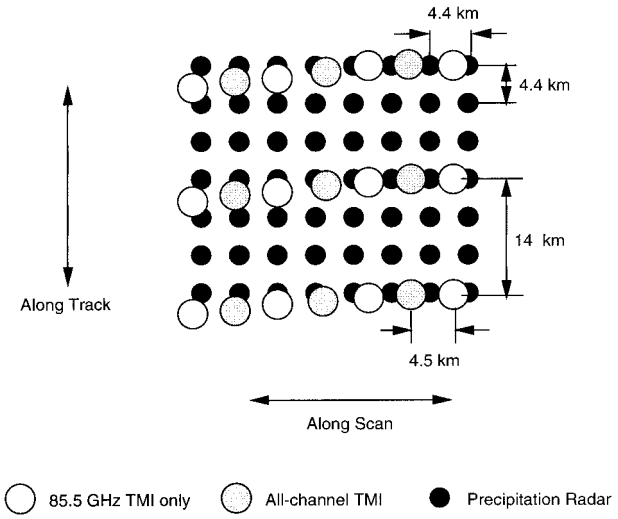

FIG. 11. Scan geometry of TMI and PR.

vective/stratiform separation results from PR data are compared. Figures 13 and 14 show two cases from TRMM data, one is Supertyphoon Paka on 19 December 1997 and the other is a squall line on 7 April 1998. The PR-derived rainfall rates, C/S index, and the TMI-derived convective fraction area are shown in panels a, b, and c, respectively. Rainfall rates from PR are provided by Dr. T. Iguchi at Communication Research Laboratory, Japan (1988, personal communication). Tables 5 and 6 list percentages of matched classification rainfall areas and rainfall amounts at the resolution of TMI 85-GHz channels.

It can be seen from Fig. 13 that the C/S separation using TMI data has a good agreement with that using PR data, especially in strong convective areas, such as in the hurricane eye wall. Results in Table 5 indicate that about 73.65% rainfall area that corresponds about 56.55% rainfall volume is correctly classified based on PR. The total misclassification is about 6.51% rainfall area corresponding to about 12.27% rainfall volume.

In the squall line case (Fig. 14), the TMI-derived C/S separation also show reasonable agreement with that from the PR. About 80% rainfall area representing about 58% rainfall volume has the same classification as the PR scheme. However, Fig. 14c displays less convective area than that from PR data in Fig. 14b. Table 6 shows that about 7.44% of the rainfall areas that are classified as convective by PR have been considered as either mixed or stratiform by the TMI scheme. This may be caused by the fact that there is not strong ice scattering (low 85 GHz) over this squall line (not shown in the paper).

c. Synthetic SSM/I data

Synthetic SSM/I data are produced by averaging simulated TOGA brightness temperature data at 2-km res-

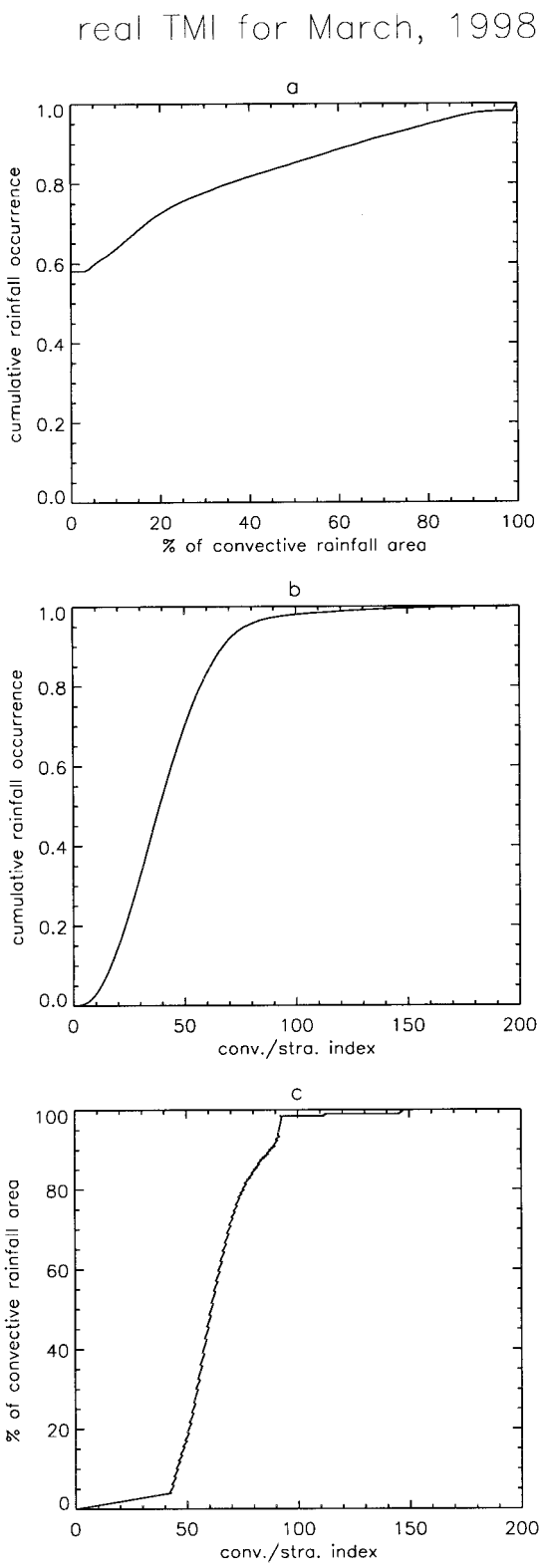

FIG. 12. Same as in Fig. 6 except that actual TMI data and PR data over oceans for Mar 1998 are used.

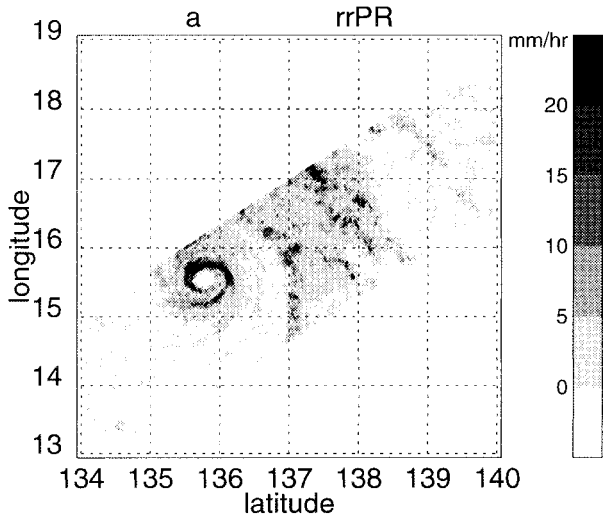

FIG. 13. Supertyphoon Paka on 19 Dec 1997. (a) The PR-derived rainfall rates; (b) the PR-derived C/S index; (c) the C/S map from actual TMI data.

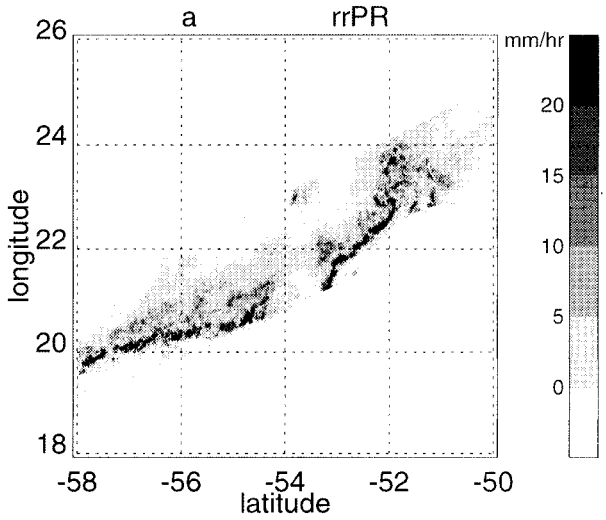

FIG. 14. Same as in Fig. 13 except for the squall line on 7 Apr 1998.

TABLE 5. Matched percentages of total rainfall areas and volumes for actual TMI data (Supertyphoon Paka on 19 Dec 1997).

PR radar reflectivity scheme	Brightness temperature scheme					
	Percent of rainfall areas			Percent of rainfall volumes		
	Convective	Mixed	Stratiform	Convective	Mixed	Stratiform
Convective	1.93	0.86	3.65	11.21	4.28	7.09
Mixed	2.12	2.99	11.35	5.76	7.78	13.96
Stratiform	2.86	5.51	68.73	5.18	7.18	37.56

olution to 14 km for 85 GHz, 22 km for 37 GHz, and 42 km for 19 GHz, respectively. Limited by resolutions, only 85-GHz data are used so that C/S separation is based solely on the scattering index of CSI_s. Cumulative rainfall histograms are created as functions of both the fraction of convective precipitation area from radar and the CSI_s from synthetic SSM/I 85-GHz data (see Figs. 15a and 15b). Unlike the CDF for TMI, the CDF of convective precipitation fraction for SSM/I increases smoothly due to a larger satellite FOV.

Like in the previous section, an SSM/I pixel is considered as convective/mixed/stratiform according to the fraction of convective precipitation in its footprint. Figures 7d–10d show C/S maps for the above four cases. An SSM/I pixel is assumed as ''raining'' as long as there is one raining radar pixel in the SSM/I FOV so that raining areas in Figs. 7d–10d are larger than those in Figs. 7a–10a. The separation results using synthetic SSM/I data are very similar to those using synthetic TMI data except that the reduced resolution causes the loss of some detailed information. For example, two heavy rain areas (around 2°S and 155°E) in the case of 16 December 1992 in Fig. 9a have only been seen as a larger mixed/convective rain area in Fig. 9d.

d. Actual SSM/I data

Real SSM/I data are those from *F10* or *F11* satellite that overpassed TOGA COARE radar sites. The SSM/I data are first screened to eliminate nonraining pixels. Histograms of CSI_s were then collected from those satellite FOVs where rain was possible and there were at least 7×7 collocated radar pixels (i.e., 14 km $\times$ 14 km). Figures 16a and 16b exhibit cumulative histograms of the fraction of convective precipitation area and the CSI_s that are slightly different from those in Figs. 16a and 16b, respectively, because of different radar samples. It can be seen that Figs. 15c and 16c are very similar although one is for synthetic SSM/I data and the other is for actual SSM/I data.

Figures 7e–10e displayed C/S maps from real SSM/I data for four TOGA cases. In areas where heavy rain is present, classifications from real SSM/I data perform quite well although the results are smeared due to low resolution. In case 4 (Fig. 10e), real SSM/I data-derived C/S map showed less convective areas than those from synthetic data (Fig. 10d). This indicates that there was very little ice aloft in the convective system although surface rain rates were high.

5. Summary and conclusions

A new scheme that classifies convective and stratiform precipitation areas over oceans using passive microwave brightness temperature has been developed. Since convective precipitation has high spatial variability as well as high intensity, the scheme makes use of multichannel brightness temperatures and the maximum variation between the central pixel and its surrounding pixels as the indicator of convection. The maximum variation is used because of the relatively low resolution of microwave brightness temperature data. Utilization of multichannel data takes advantage of the fact that emission data from low-frequency channels are physically related to rainfall while scattering data from high-frequency channels have high resolution. The addition of 37-GHz data also provides information regarding cloud liquid water. The C/S index works particularly well for those data of which the resolution is equivalent to or larger than the scale of convection.

Since lower-resolution satellite data generally contain mixtures of convective and stratiform precipitation, a probability matching method is employed to relate a C/S index to a convective precipitation fraction. Although this algorithm is developed for TMI data, it can be applied to the SSM/I data too after the C/S index is

TABLE 6. Matched percentages of total rainfall areas and volumes for actual TMI data (squall line on 7 Apr 1998).

PR radar reflectivity scheme	Brightness temperature scheme					
	Percent of rainfall areas			Percent of rainfall volumes		
	Convective	Mixed	Stratiform	Convective	Mixed	Stratiform
Convective	1.53	3.35	4.09	8.56	13.89	10.72
Mixed	0.12	2.87	10.78	0.31	5.62	16.01
Stratiform	0.00	0.98	76.27	0.00	1.08	43.82

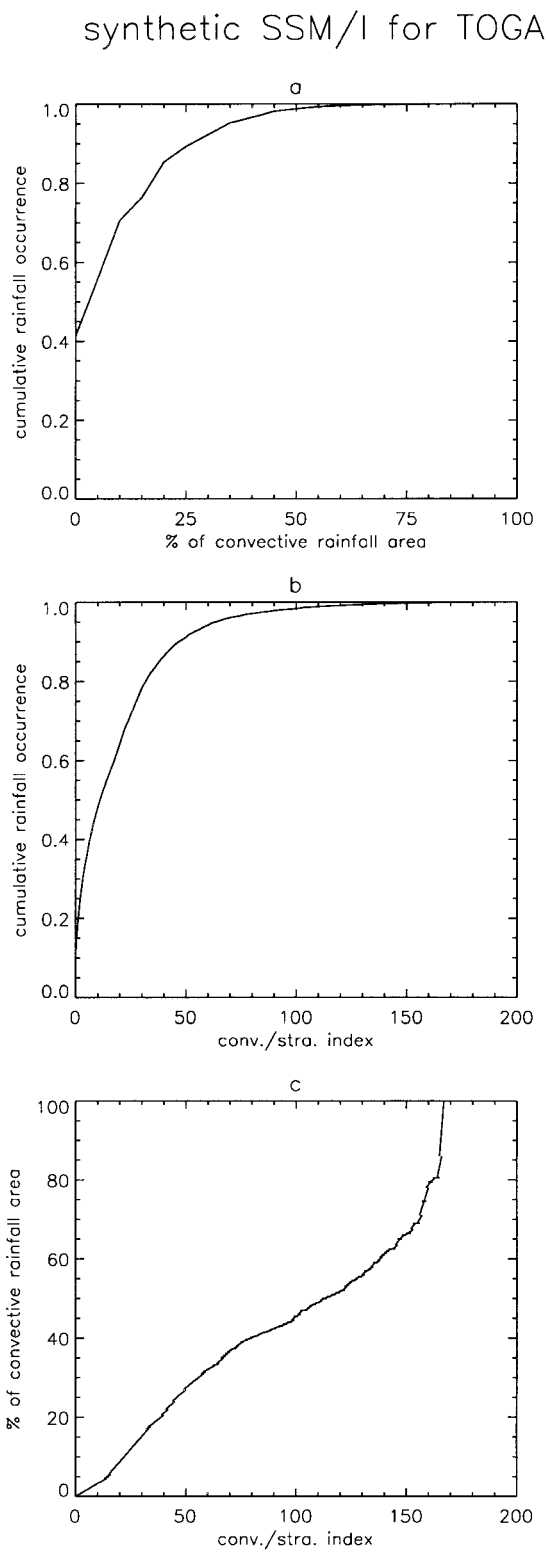

FIG. 15. Same as in Fig. 6 except for synthetic SSM/I data.

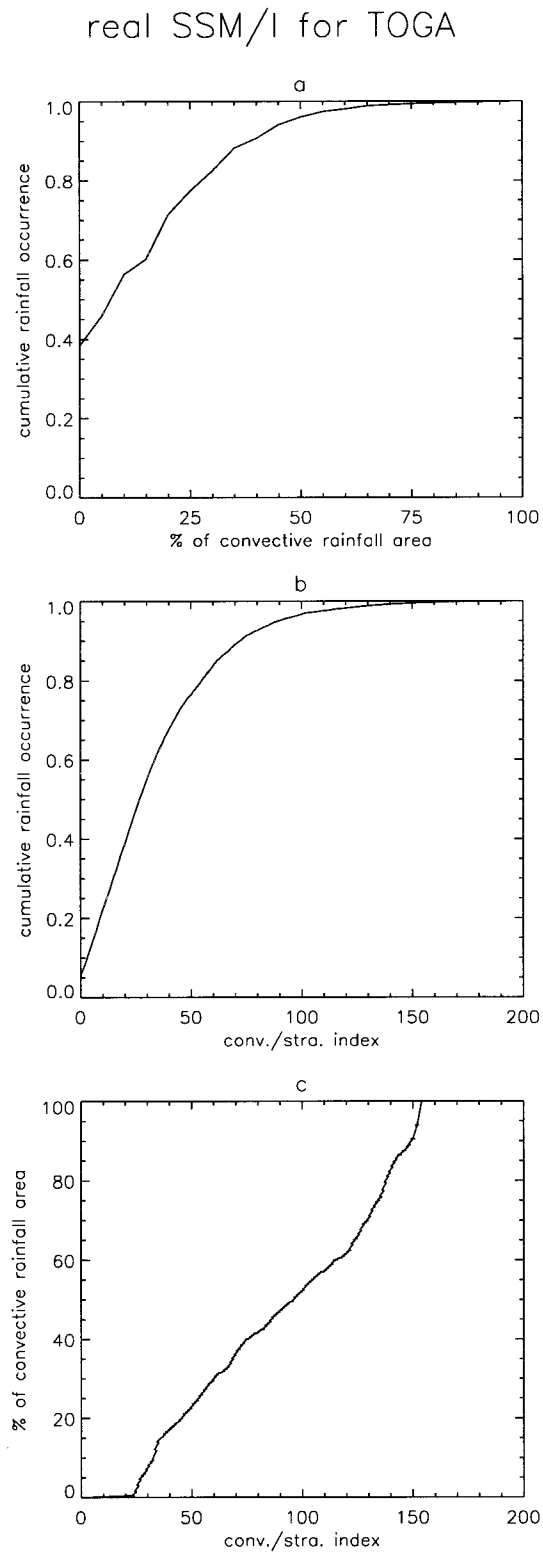

FIG. 16. Same as in Fig. 6 except for actual SSM/I data.

modified and the cumulative distribution functions of precipitation are reconstructed based on SSM/I's resolutions.

This C/S separation scheme has been tested on both synthetic and real TMI data, as well as synthetic and actual SSM/I data. Classification results have been validated against ground-based and spaceborne radar data. Results from synthetic TMI data agree with C/S maps from radar very well for organized convective systems. For embedded convective precipitation within stratiform precipitation, however, T_{B19} and T_{B37} become saturated and offer little guidance. The scheme still works well only if there is enough ice in the cloud so that T_{B85} shows a significant depression.

Although the scheme was developed using model-based synthetic TMI data before the launch of TRMM satellite, comparison of real TMI data derived C/S separation with that from PR data has shown very encouraging results. Due to the ongoing improvements to TRMM products, very limited results are available for the present study. Validation of the scheme against PR data on a global basis and improvement of the scheme are expected.

Acknowledgments. The authors would like to thank Drs. David Short, Brad Ferrier, and Tom Bell for helpful discussions. The help of Drs. Toshio Iguchi and Jun Awaka in providing preliminary TRMM radar data analysis is gratefully appreciated. We also thank two anonymous reviewers for their constructive comments and suggestions. This work is supported by the TRMM science program.

REFERENCES

Adler, R. F., and A. J. Negri, 1988: A satellite infrared technique to estimate tropical convective and stratiform rainfall. *J. Appl. Meteor.,* **27,** 30–51.

Alishouse, J. C., J. B. Snider, E. R. Westwater, C. T. Swift, C. S. Ruf, S. A. Snyder, J. Vongsathorn, and R. R. Ferraro, 1990: Determination of cloud liquid water content using SSM/I. *IEEE Trans. Geosci. Remote Sens.,* **28,** 817–822.

Anagnostou, E. N., and C. Kummerow, 1997: Stratiform and convective classification of rainfall using SSM/I 85-GHz brightness temperature observations. *J. Atmos. Oceanic Technol.,* **14,** 570–575.

Calheiros, R. V., and I. Zawadzki, 1987: Reflectivity rain-rate relationships for radar hydrology in Brazil. *J. Climate Appl. Meteor.,* **26,** 118–132.

Churchill, D. D., and R. A. Houze Jr., 1984: Development and structure of winter monsoon cloud clusters on 10 December 1978. *J. Atmos. Sci.,* **41,** 933–960.

Collier, C. G., S. Lovejoy, and G. L. Austin, 1980: Analysis of bright bands from 3D radar data. Preprints, *19th Conf. on Radar Meteorology,* Miami Beach, FL, Amer. Meteor. Soc., 44–47.

Durden S. L., E. Im, F. K. Li, W. Ricketts, A. Tanner, and W. Wilson, 1994: ARMAR: An Airborne Rain-Mapping Radar. *J. Atmos. Oceanic Technol.,* **11,** 727–737.

Ferrier, B. S., J. C. Gerlach, P. A. Kucera, D. A. Short, A. A. Rutledge, J. Lutz, and O. W. Thiele, 1995: Corrections and comparisons of TOGA COARE shipborn radar reflectivities. Preprints, *27th Conf. on Radar Meteorology,* Vail, CO, Amer. Meteor. Soc., 675–677.

Greenwald, T. J., G. L. Stephens, T. H. Vonder Haar, and D. L. Jackson, 1993: A physical retrieval of cloud liquid water over the global oceans using special sensor microwave/imager (SSM/I) observations. *J. Geophys. Res.,* **98,** 18 471–18 488.

Houze, R. A., Jr., 1989: Observed structure of mesoscale convective systems and implications for large-scale heating. *Quart. J. Roy. Meteor. Soc.,* **115,** 425–461.

——, 1993: *Cloud Dynamics.* Academic Press, 573 pp.

Kucera, P. A., and Coauthors, 1995: COARE IOP rainfall from shipborne radars: 1. Analysis and comparison of gridded fields. Preprints, *27th Conf. on Radar Meteorology,* Vail, CO, Amer. Meteor. Soc., 681–683.

Kummerow, C., 1997: Beamfilling errors in passive microwave rainfall retrievals. *J. Appl. Meteor.,* **37,** 356–370.

——, and L. Giglio, 1994a: A passive microwave technique for estimating rainfall and vertical structure information from space. Part I: Algorithm description. *J. Appl. Meteor.,* **33,** 3–18.

——, and ——, 1994b: A passive microwave technique for estimating rainfall and vertical structure information from space. Part II: Applications to SSM/I data. *J. Appl. Meteor.,* **33,** 19–33.

Leary, C. A., and R. A. Houze Jr., 1979: The structure and evolution of convection in a tropical cloud cluster. *J. Atmos. Sci.,* **36,** 437–457.

Liu, G., J. A. Curry, and R.-S. Sheu, 1995: Classification of clouds over the western equatorial Pacific ocean using combined infrared and microwave satellite data. *J. Geophys. Res.,* **100,** 13 811–13 826.

McCumber, M., W.-K Tao, J. Simpson, R. Penc, and S.-T. Soong, 1991: Comparison of ice-phase microphysical parameterization schemes using numerical simulations of convection. *J. Appl. Meteor.,* **30,** 985–1004.

McGaughey, G., E. J. Zipser, R. W. Spencer, and R. E. Hood, 1996: High resolution passive microwave observations of convective systems over the tropical Pacific Ocean. *J. Appl. Meteor.,* **35,** 1921–1947.

Mugnai, A., E. A. Smith, and G. J. Tripoli, 1993: Foundations for statistical-physical precipitation retrieval from passive microwave satellite measurements. Part II: Emission-source and generalized weighting-function properties of a time-dependent cloud-radiation model. *J. Appl. Meteor.,* **32,** 17–39.

Reynolds, D. W., and T. H. Vonder Haar, 1977: A bispectral method of cloud parameter determination. *Mon. Wea. Rev.,* **105,** 446–457.

Rosenfeld, D., D. B. Wolff, and D. Atlas, 1993: General probability-matched relations between radar reflectivity and rain rate. *J. Appl. Meteor.,* **32,** 50–72.

——, E. Amitai, and D. B. Wolff, 1995: Classification of rain regimes by the three-dimensional properties of reflectivity fields. *J. Appl. Meteor.,* **34,** 198–211.

Rossow, W. B., and R. A. Schiffer, 1991: ISCCP cloud data products. *Bull. Amer. Meteor. Soc.,* **72,** 2–20.

Shenk, W. E., R. J. Holub, and R. A. Neff, 1976: A multispectral cloud type identification method using Nimbus-3 MRIR measurements. *Mon. Wea. Rev.,* **104,** 284–291.

Short, D. A., P. A. Kucera, B. S. Ferrier, and O. W. Thiele, 1995: COARE IOP rainfall from shipborne radars: 1. Rain mapping algorithms. Preprints, *27th Conf. on Radar Meteorology,* Vail, CO, Amer. Meteor. Soc., 678–680.

Simpson, J. R., R. Adler, and G. R. North, 1988: A proposed tropical rainfall measuring mission (TRMM). *Bull. Amer. Meteor. Soc.,* **69,** 278–295.

Smith, E. A., A. Mugnai, H. J. Cooper, G. J. Tripoli, and X. Xiang, 1992: Foundations for statistical physical precipitation retrieval from passive microwave satellite measurements. Part I: Brightness temperature properties of a time-dependent cloud radiation model. *J. Appl. Meteor.,* **31,** 506–531.

Spencer, R. W., R. E. Hood, F. J. LaFontaine, E. A. Smith, J. Galliano, and E. Lobl, 1994: High resolution imaging of rain systems with the advanced microwave precipitation radiometer. *J. Atmos. Oceanic Technol.,* **11,** 849–857.

Steiner, M., and R. A. Houze Jr., 1993: Three-dimensional validation

at TRMM ground truth sites: Some early results from Darwin, Australia. Preprints, *25th Conf. on Radar Meteorology*, Norman, OK, Amer. Meteor. Soc., 417–420.

——, ——, and S. E. Yuter, 1995: Climatological characterization of three-dimensional storm structure from operational radar and rain gauge data. *J. Appl. Meteor.*, **34,** 1978–2007.

Tao, W.-K., and J. Simpson, 1989: Modeling study of a tropical squall-type convective line. *J. Atmos. Sci.,* **46,** 172–202.

——, and ——, 1993: Goddard Cumulus Ensemble model. Part I: Model description. *TAO,* **4,** 35–72.

——, ——, C.-H. Sui, S. Lang, J. Simpson, and R. Adler, 1993: Retrieval algorithms for estimating the vertical profiles of latent heat release: Their applications for TRMM. *J. Meteor. Soc. Japan,* **71,** 685–700.

Yuter, S. E., and R. A Houze Jr., 1995: Three-dimensional kinematic and microphysical evolution of Florida cumulonimbus. Part II: Frequency distributions of vertical velocity, reflectivity and differential reflectivity. *Mon. Wea. Rev.,* **123,** 1941–1963.

Zipser, E. J., 1977: Mesoscale and convective-scale downdrafts as distinct components of squall-line circulation. *Mon. Wea. Rev.*, **105,** 1568–1589.